Article

Talbot Effect in InAs/GaAs Coupled Cylindrical Quantum Dots Ensemble

Paytsar Mantashyan[1,2], Grigor Mantashian[2,1]* and David Hayrapetyan[2,1]

[1] Institute of Chemical Physics after A.B. Nalbandyan of NAS RA, 5/2 Paruyr Sevak St., Yerevan 0014, Armenia; paytsar.mantashyan@gmail.com
[2] Department of General Physics and Quantum Nanostructures, Russian-Armenian University, 123 Hovsep Emin Str., Yerevan 0051, Armenia; paytsar.mantashyan@gmail.com, david.hayrapetyan@rau.am
* Correspondence: grigor.mantashyan@rau.am

Abstract: Talbot effect is a self-imaging or lensless imaging phenomenon of a periodic grating illuminated by a collimated light beam at regular distances from the grating. Research on the Talbot effect has recently made significant strides thanks to the quick development of optical superlattices. The emergence of various applications of this effect in fields such as optics, acoustics, X-ray, plasmonics, and information processing has led to the increasing importance of obtaining a Talbot carpet with the use of different structures. In this paper, we investigate the Talbot effect that originates from the tunneling effect between an ensemble of vertically coupled cylindrical $InAs/GaAs$ quantum dots (QDs). The Talbot carpet can be manipulated by changing the parameters of the QD system. In the current paper, two modified Pöschl-Teller potentials were used to model the QDs ensemble. The exciton's lifetime and tunneling time's dependence on the first QD's potential half-width is found for a fixed value of the external electric field. The nonlinear changes in the refractive index and absorption spectrum dependent on the tunneling effect are obtained. Afterward, the Talbot carpet formation is investigated, particularly the dependences of the formed periodic wavefront's visibility on medium length, coupling field's strength, and tunneling parameter. Finally, we have observed the intensity distribution of the diffraction field at Talbot half-distance.

Keywords: coupled quantum dots; InAs/GaAs; tunneling effect; exciton; biexciton; Talbot effect; optical lattice

1. Introduction

The Talbot effect is a self-imaging phenomenon of a periodic grating illuminated by a collimated light beam at regular distances (Talbot length) from the grating. It was discovered in 1836 [1]. The effect takes place in the near-field diffraction regime. Due to this effect, a self-replication of the grating occurs, and half-period phase-shifted copies of the light distribution are created at the Talbot half-distances. These repeated images are called Talbot images. Talbot images' distribution in the longitudinal direction is called a Talbot carpet.

Due to the considerable rise of the interest mediated by various applications of the effect, such as photolithography [2,3], interferometry [4,5], quantum information [6,7], etc., its attainment from different structures remains a valid problem. One of the main challenges of the Talbot effect is obtaining high-resolution images reproducible at the fractional-Talbot planes. Besides initially used diffraction gratings, various periodic structures such as photonic crystals [8,9], graphene [10], refractive gratings [11], and bosonic atoms [12] have been to observe high-resolution Talbot images both experimentally and theoretically.

Semiconductor QDs have become an important platform for the fields of quantum and non-linear optics due to their controllable optical properties. QDs have discrete energy levels similar to natural atoms. However, unlike the atoms, the position of the levels and their optical selection rules are not solely determined by the material but also by

Preprints (www.preprints.org) | NOT PEER-REVIEWED | Posted: 27 December 2022 doi:10.20944/preprints202212.0505.v1

something called the size quantization effect. The size quantization can be controlled by adjusting the size, morphology, and composition of the QDs during the growth process. Due to this fact, a plethora of controllable growth techniques have been developed to artificially structure QDs with different sizes, shapes, and geometries. The combination of the abovementioned facts leads to the ability to obtain QD systems with virtually any emission wavelengths. These peculiarities are what make QDs a family of very prominent materials with a wide range of applications, which include biomedicine [13], energy harvesting [14], displays [15, 16], quantum information processing [17], etc. Coupled QD ensembles have different properties from single QDs. Factors such as the ratio of the geometrical parameters of coupled structures, interdot distance as well as diffusion all come into play and give additional degrees of freedom for the control of the system's final parameters. Self-assembled three-dimensional islands of *InAs* grown on a *GaAs* substrate, in particular, are promising candidates for photonic applications, such as QD light-emitting diodes [16], and QD lasers [18]. It was shown that the growth of the self-assembled structures can be manipulated to form single layers of QDs with well-defined excited state transitions. The energy levels of such QD systems can be controlled to match the number of confined states and their inter-sublevel energy distances [19, 20].

The seminal work related to the production of a controllable Talbot phenomenon using a QDs ensemble was performed in Ref. [21]. The authors investigated the Talbot effect that occurs at the exit plane of the system. It was shown that intensity patterns can be manipulated by the quantum dot's parameters, in particular, the tunneling parameter. However, this work lacked detailed and realistic modeling of the QDs from a material science perspective.

In this paper, we will investigate the occurrence of the Talbot effect caused by an ensemble of vertically coupled $InAs/GaAs$ cylindrical QDs ensemble. For the first time, one (exciton) and two (biexciton) electron-hole pair transitions in the vertically coupled cylindrical QDs ladder-type system, will be considered for the realization of the Talbot effect from the perspective of the solid-state physics. The dependence of the exciton lifetime and tunneling time on the half-width of the first quantum dot will be found for the fixed value of the external electric field. The dependences of the nonlinear refractive index changes and the nonlinear absorption spectrum on the tunneling effect will be explored. Next, the formation of the Talbot carpet will be investigated in detail. An analysis of the dependences of the periodic wavefront's visibility on the medium length, the coupling field's strength, and the tunneling parameter will be presented. Finally, we will attain the intensity distribution of the diffraction field at Talbot half-distance.

The paper will have the following organization, in Section 2 the materials and methods will be introduced. Section 3 results and discussions will be given with subsections, the exciton lifetime and tunneling time, the interaction of optical probe and coupling fields with QDs ensemble, and tunneling induced Talbot effect will be presented. The final Section 4 is the conclusion.

2. Materials and Methods

We have chosen $InAs$ as the QD material and $GaAs$ as the matrix material for our calculations. Vertically coupled cylindrical QD systems were modeled for the mentioned materials. The system consisting of two neighboring cylindrical dots, that have different heights, and the corresponding energy band diagram are presented in Figure 1. The following material parameters have been used in the calculations: $m^* = 0.023m_0$, where m_0 is the free electron mass, $\varepsilon = 15.15$ is dielectric susceptibility, the energy band gap of bulk $InAs$ is $E_g^{InAs} = 0.415eV$ and for $GaAs$ is $E_g^{InAs} = 1.519eV$. The confinement potential height for the electron and hole, respectively, are $U_e = 0.644eV$ and $U_h = 0.46eV$ [22].

An electron-hole pair can be excited in the first dot by a near-resonant interband probe field. Then, with the help of an applied electric field the tunneling of the conduction band's electron from the first QD to the second one can be implemented. Thus, forming an indirect exciton in the system. And finally, a second exciton (direct) is excited

Preprints (www.preprints.org) | NOT PEER-REVIEWED | Posted: 27 December 2022 doi:10.20944/preprints202212.0505.v1

in the first QD by the resonant interband coupling field. Thus, probe and coupling optical fields will be applied to the system to generate interband transitions in QD. So, to model this process we first have to obtain the excitonic states of the system in the presence of an external electric field $\vec{F}(0,0,F_z)$.

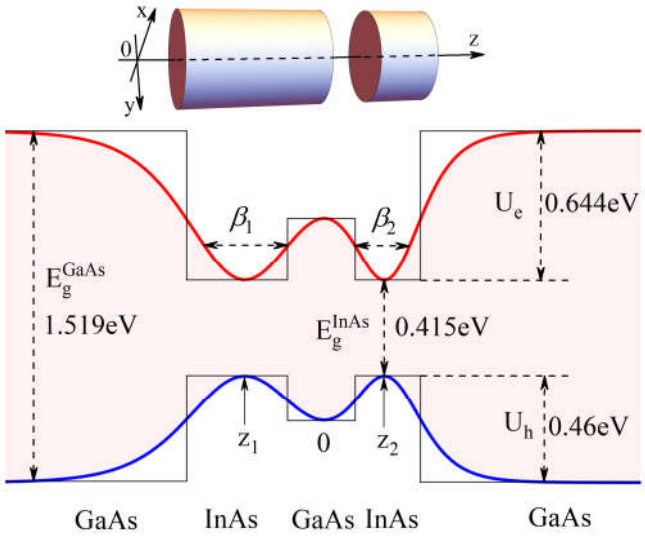

Figure 1. Energy band diagram of $InAs/GaAs$ coupled cylindrical QDs system. As the confinement potential, two modified Pöschl-Teller potentials have been used with β_1 and β_2 half widths, and with z_1 and z_2 center coordinates. The confinement potential height U_e and U_h for the electron and hole respectively, have been estimated from the $InAs/GaAs$ band structure engineering.

We have chosen the sum of well-known modified Pöschl-Teller potentials (MPTP) [23-25] as the confinement potential for the axial direction. Traditionally, a finite rectangular potential well was used to describe the effect of the QDs confinement on the charge carriers. However, because of the diffusion during the growth process between QD's material and surrounding media, the confinement potential of vertically coupled QDs is better approximated by a smoother potential [26]. The authors of [26] have calculated how a spherical In_xGa_xAs QD embedded in $GaAs$ changed the potential and confinement energy by inter-diffusion. Compared to a quantum well, the potential decreases more quickly as the diffusion length around a QD increases. Their findings suggest that regular inter-diffusion interactions between the dots and surrounding medium can account for the observed reduction of the photoluminescence linewidth that happens as a result of the rapid thermal annealing of self-assembled $InAs$ QD structures.

In the radial direction, the parabolic potential has been chosen, since we will consider the tunneling between the QDs only in the axial direction. Note, that the MPTP turns into a parabolic potential in the limit and for the lower energy levels the values for MPTP and parabolic potential are the same.

The analytical form of the confinement potential for the electron (hole) in axial and radial directions in cylindrical coordinates has the following form:

$$\begin{cases} U_{e(h)}^{conf}\left(z_{e(h)}\right) = 2U_{e(h)} - \dfrac{U_{e(h)}}{\cosh^2\left(\dfrac{z_{e(h)}+z_1}{\beta_1}\right)} - \dfrac{U_{e(h)}}{\cosh^2\left(\dfrac{z_{e(h)}-z_2}{\beta_2}\right)}, \\ U_{e(h)}^{conf}\left(\rho_{e(h)}\right) = \dfrac{m_{e(h)}^{*}\omega_{e(h)}^{2}}{2}\rho_{e(h)}^{2}, \end{cases} \quad (1)$$

Preprints (www.preprints.org) | NOT PEER-REVIEWED | Posted: 27 December 2022 doi:10.20944/preprints202212.0505.v1

where $U_{e(h)}$ is the potential depth of the MPTP for the electron (hole), $\beta_{1(2)}$ - are the half widths and $z_{1(2)}$ are the centers for the first and second QDs, $m^*_{e(h)}$ is electron effective mass, $\omega_1 = \omega_2 \equiv \omega$ is the parabolic potential parameter. The half-width $\beta_{1(2)}$ is related to the cylinder height H_{cyl} by the relation $\beta = \lambda_{ax} H_{cyl}$. And the ω parameter is related to the cylinder radius R by the relation $\omega_e = \lambda_{rad} \frac{\hbar}{m^*_{e(h)} R^2}$, here λ_{ax}, and λ_{rad} are empirically defined prefactors. We can see in Figure 1 the MPTP is overlaid on the rectangular quantum well in such a way that the $\beta_{1(2)}$ parameter closely matches the cylinder's height as a result the λ_{ax} approximately becomes 1. Interdot distance between two QDs is defined as the distance between centers of the QDs z_1 and z_2. In our case, we consider two cylindrical QDs with heights corresponding to $\beta_1 = 20nm$ and $\beta_2 = 10nm$, with an interdot distance of $10nm$, which means $25nm$ between centers.

As we mentioned above, at the first stage, the system has been radiated with the near-resonant interband probe field. Which leads to an excitation of a bound electron hole pair. The Hamiltonian operator of the exciton in a vertically coupled QD system can be written as:

$$\hat{H}_X = \hat{H}_e + \hat{H}_h + U_e^{conf} + U_h^{conf} + V_{\text{int}}. \quad (2)$$

Here $\hat{H}_{e(h)}$ is the kinetic part of the Hamiltonian for the electron (hole) and is equal to

$$\hat{H}_{e(h)} = -\frac{\hbar^2}{2m^*_{e(h)}} \nabla^2_{e(h)}. \quad (3)$$

The terms of the confinement potential for the particles can be presented as a sum of the axial and radial parts:

$$U^{conf}_{e(h)} = U^{conf}_{e(h)}\left(z_{e(h)}\right) + U^{conf}_{e(h)}\left(\rho_{e(h)}\right). \quad (4)$$

And finally, the last term represents interparticle Coulomb interaction:

$$V_{\text{int}} = -\frac{e^2}{\varepsilon |\vec{r}_e - \vec{r}_h|}. \quad (5)$$

where ε is the dielectric constant.

In the second stage, the external electric field is applied to the system in an axial direction. Which leads to the addition of new terms in the Hamiltonian. The terms in Hamiltonian corresponding to the external electric field can be presented in this form:

$$V_e^{el} + V_h^{el} = -eF_z z_e + eF_z z_h. \quad (6)$$

Let us recall that the electron-hole pair is generated under the effect of the probe field $\hbar\omega_p$ which has an interband near-resonant character. The exciton eigenproblem has been solved with the help of the variational method using single-particle wave functions and energies to construct trial wave function, and by minimization of the following integral:

$$E_X = \left\langle \Psi_{trial}(\vec{r}_e, \vec{r}_h) \middle| \hat{H}_X \middle| \Psi_{trial}(\vec{r}_e, \vec{r}_h) \right\rangle. \quad (7)$$

where

$$\Psi_{trial}(\vec{r}_e, \vec{r}_h) = \psi_e(\vec{r}_e)\psi_h(\vec{r}_h)\exp\left[-\lambda_{\text{var}} \frac{|\vec{r}_e - \vec{r}_h|}{a_B}\right]. \quad (8)$$

Here λ_{var} is a variational parameter. The charge carrier wave function $\psi_{e(h)}\left(\vec{r}_{e(h)}\right)$ can be presented as a product of axial and radial parts $\psi_{e(h)}\left(\vec{r}_{e(h)}\right) = R\left(\rho_{e(h)}, \varphi_{e(h)}\right)\chi\left(z_{e(h)}\right)$, moreover, the radial part is solved analytically. Because the double MPTP in the axial direction cannot be solved analytically the solution of the single particle eigenproblem was performed with the use of the finite element method (FEM).

Due to the asymmetric character of the system, the ground state energy of the electron (hole) in the second QD is higher than the ground state energy of the electron (hole)

Preprints (www.preprints.org) | NOT PEER-REVIEWED | Posted: 27 December 2022 doi:10.20944/preprints202212.0505.v1

in the first QD. The ground state energies of electron and hole in the first and second QDs without external electric field are $E_e^1 = 53.4meV$, $E_e^2 = 106.7meV$, $E_h^1 = 29.1meV$ and $E_h^2 = 41.6meV$ (see Figure 2 (a)). We indicate indexes 1 and 2 correspondingly for the left and right QDs. With the application of the external electric field, the confinement potential becomes modified and the energy levels shift in contrast to the initial position. We carefully chose the external electric field magnitude, to equalize the energies of the electron in the first and second QDs. For the $F = 47.8V/cm$ case the shifted energy levels will have the following values: $E_e^1 = E_e^2 = 92.98meV$, $E_h^1 = 56.21meV$ and $E_h^2 = 70.88meV$.

Note that, for the hole the difference between energies in the first and second QDs increases, which leads to a decrease in the possibility of the hole's tunneling through the barrier (see Figure 2 (b)). Hence the conduction-band levels are in a resonance regime, while the valance-band levels are in the off-resonance regime. In this way, we will have an effective coupling between the electron levels and decoupling between the hole levels respectively. Based on the state of the system described above, we can neglect the tunneling effect connected with the hole, so only tunneling with the electron will be considered. After the tunneling, the second exciton will be excited with the help of a resonant interband optical pulse $\hbar\omega_c$ (see Figure 2 (c)). Consequently, a formation of a biexciton state will occur. Thus, in this current manuscript, we will consider the four-level ladder-type system.

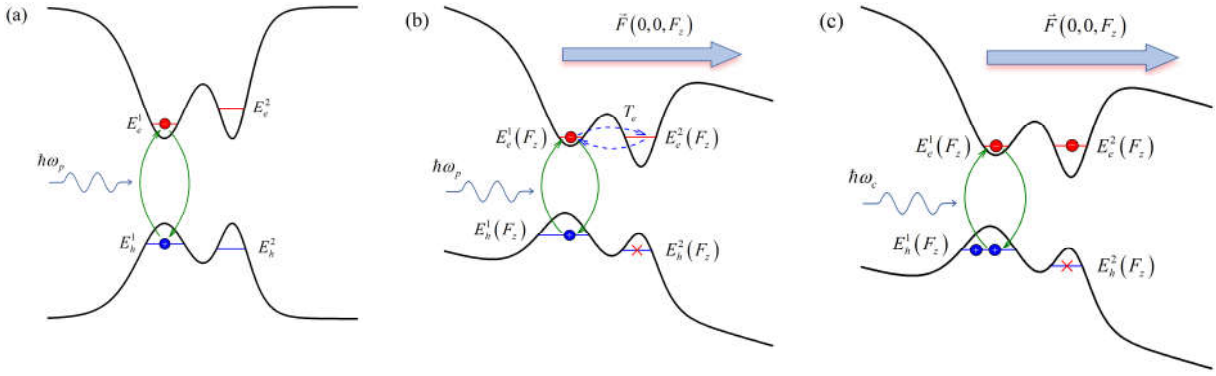

Figure 2. Energy band diagram of $InAs/GaAs$ coupled cylindrical quantum dots system and creation of electron-hole pair under the influence of near resonant interband probe field without (a) and with (b) external electric field directed with the axial axes, (c) creation of second electron-hole pair under the influence of near resonant interband coupling field.

3. Results and discussion

3.1. The exciton lifetime and tunneling time

In order to have the opportunity for tunneling between the QDs, the electron-hole recombination time should be longer than the tunneling time. Thus, the exciton lifetime and tunneling time should be estimated and compared with each other to understand the possibility of the realization of a four-level system. To estimate the exciton recombination time, we use the formula obtained in [27]:

$$\tau_{exc} = \frac{2\pi\varepsilon_0 m_0 c^3 \hbar^2}{\sqrt{\varepsilon} e^2 E_{exc}^2 f}. \tag{9}$$

where ε_0 is vacuum permittivity, m_0 is the mass of the free electron, E_{exc} is the energy of an exciton and f is the oscillator strength, which is defined by the formula:

$$f = \frac{E_K}{E_{exc}} \left| \int_V \Psi_{exc}(\vec{r}_e, \vec{r}_h) d\vec{r} \right|^2. \tag{10}$$

Preprints (www.preprints.org) | NOT PEER-REVIEWED | Posted: 27 December 2022 doi:10.20944/preprints202212.0505.v1

Here $\Psi_{exc}(\vec{r}_e,\vec{r}_h)$ is the exciton wave function, E_K which is the Kane energy, and for $InAs$ it is $E_K = 21.5eV$ [28]. Next, to obtain the tunneling time we will use the relation obtained for the tunneling rate between two QDs which is defined by the equation [29,30]:

$$\Gamma_{tun} = \left(\frac{4U_e\beta}{\pi\hbar}\right)^2 \sqrt{\frac{\beta^2 m_e^*}{2E_e^1}} \exp\left\{-\frac{4}{3}\frac{\sqrt{2m_e^*}}{\hbar e F_z}\left(E_e^1\right)^{\frac{3}{2}}\right\}. \quad (11)$$

where E_e^1 electron energy. The tunneling time is inversely proportional to the tunneling rate $\tau_{tun} = 1/\Gamma_{tun}$. Direct calculation shows that the exciton lifetime lies in the *ns* range, while the tunneling time lies in the *ps* range. The dependences of these relevant times on the length of the QDs system are shown in Figure 3. Exciton lifetime dependence displays linear growth behavior, while tunneling time exhibits exponential decrease behavior. Note, that dependence of the tunneling time on the electric field has a clear $\exp(-1/F_z)$ form. Thus, the consideration of the tunneling process in the current system is logical.

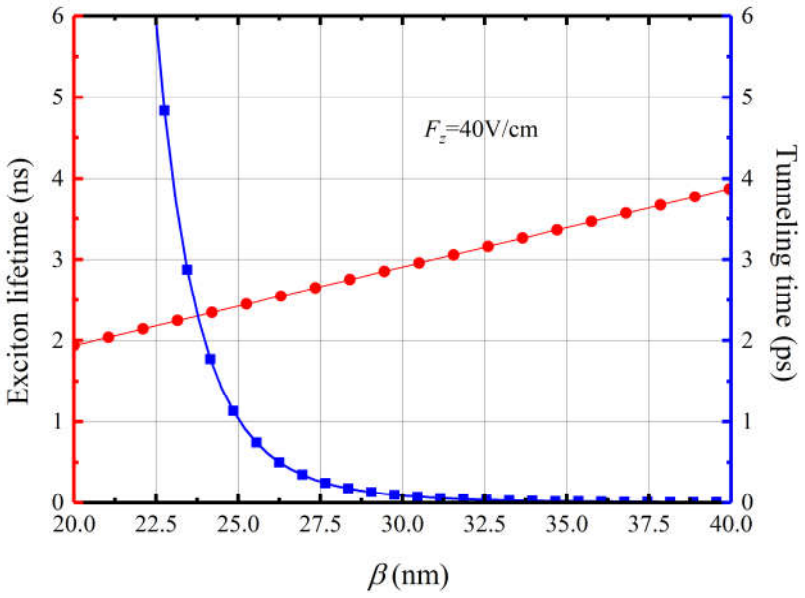

Figure 3. Dependence of the exciton lifetime and tunneling time on the half width of first QD for the fixed value of external electric field.

The four levels of the ladder type system are described in the following section. A ground state $|0\rangle$ of the system is taken to be the state where the electron-hole pair is not yet generated. The first excited state $|1\rangle$ is taken to be the state when the electron-hole pair is localized in the first QD (direct exciton). As the second excited state $|2\rangle$, a state is taken where the hole is localized in the first QD and the electron is in the second QD (indirect exciton). And finally, the third excited state $|3\rangle$ is defined by the direct and indirect excitons (biexciton) in a vertically coupled QD system (Figure 4).

Thus, the biexciton in the coupled QD system should be considered. The Hamiltonian of the biexciton confined in a vertically coupled QD system can be written as

$$H_{XX}^{次}(\vec{r}_1,\vec{r}_2,\vec{r}_\alpha,\vec{r}_\beta) = \sum_j H_j + \sum_j U_j^{conf} + \sum_j V_j^{el} + V_{\text{int}}(\vec{r}_1,\vec{r}_2,\vec{r}_\alpha,\vec{r}_\beta). \quad (12)$$

where $j = \{1,2,\alpha,\beta\}$, $\vec{r}_1$ and $\vec{r}_2$ are electrons' coordinates, $\vec{r}_\alpha$ and $\vec{r}_\beta$ —holes' coordinates. Interparticle interaction energy term $V_{\text{int}}(\vec{r}_1,\vec{r}_2,\vec{r}_\alpha,\vec{r}_\beta)$ in the Hamiltonian includes all interactions between electrons, holes, and between electrons and holes. This interaction has the following forms:

Preprints (www.preprints.org) | NOT PEER-REVIEWED | Posted: 27 December 2022 doi:10.20944/preprints202212.0505.v1

$$V_{\text{int}}\left(\vec{r}_1,\vec{r}_2,\vec{r}_\alpha,\vec{r}_\beta\right)=\frac{e^2}{\varepsilon\left|\vec{r}_1-\vec{r}_2\right|}+\frac{e^2}{\varepsilon\left|\vec{r}_\alpha-\vec{r}_\beta\right|}-\frac{e^2}{\varepsilon\left|\vec{r}_1-\vec{r}_\alpha\right|}-\frac{e^2}{\varepsilon\left|\vec{r}_1-\vec{r}_\beta\right|}-\frac{e^2}{\varepsilon\left|\vec{r}_2-\vec{r}_\alpha\right|}-\frac{e^2}{\varepsilon\left|\vec{r}_2-\vec{r}_\beta\right|}. \quad (13)$$

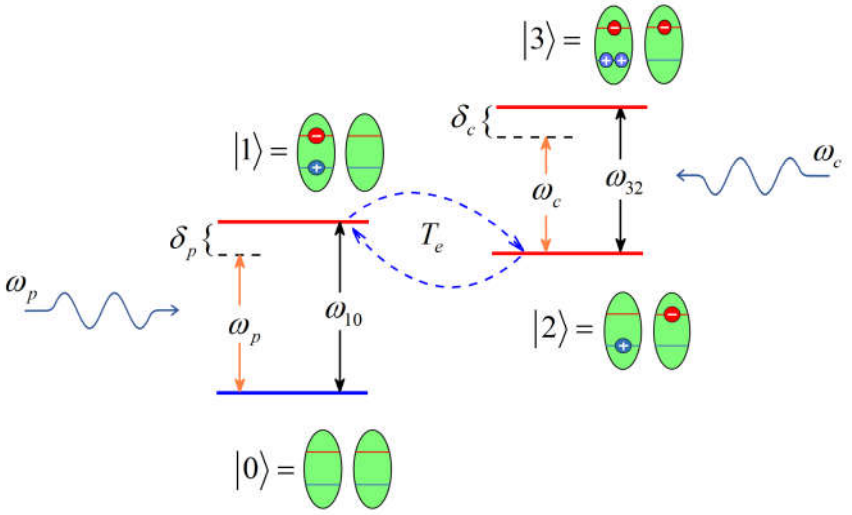

Figure 4. The energy diagram of the four-level ladder-type $InAs/GaAs$ coupled cylindrical QDs system.

The four-particle problem can be solved with the help of the variational method [31,32] using single-particle wave functions and energies to construct trial wave function and by the minimization of the following integral:

$$E_{XX}=\left\langle\Psi_{trial}(\vec{r}_1,\vec{r}_2,\vec{r}_\alpha,\vec{r}_\beta)\middle|\hat{H}_{XX}\middle|\Psi_{trial}(\vec{r}_1,\vec{r}_2,\vec{r}_\alpha,\vec{r}_\beta)\right\rangle. \quad (14)$$

$$\Psi_{trial}(\vec{r}_1,\vec{r}_2,\vec{r}_\alpha,\vec{r}_\beta)=C\psi_e(\vec{r}_1)\psi_e(\vec{r}_2)\psi_h(\vec{r}_\alpha)\psi_h(\vec{r}_\beta)\times \times e^{-\lambda^1_{\text{var}}r_{\alpha\beta}}\left\{e^{-\lambda^2_{\text{var}}(r_{1\alpha}+r_{2\beta})-\lambda^3_{\text{var}}(r_{1\beta}+r_{2\alpha})}+e^{-\lambda^2_{\text{var}}(r_{1\beta}+r_{2\alpha})-\lambda^3_{\text{var}}(r_{1\alpha}+r_{2\beta})}\right\}, \quad (15)$$

where C - normalization constant, $r_{jk}=\left|\vec{r}_j-\vec{r}_k\right|$, $j,k=\{1,2,\alpha,\beta\}$, λ^1_{var}, λ^2_{var} and λ^3_{var} are variational parameters.

3.2. Interaction of optical probe and coupling fields with QDs ensemble

Let us consider a layered medium with a length L, where each layer consists of a single column of horizontally stacked vertically coupled cylindrical QD systems (Figure 5). The vertically coupled cylindrical QD systems have the following parameters: two QDs with $20nm$ and $10nm$ heights and $10nm$ interdot distances. To avoid carrier tunneling between systems the distance between each layer is taken to be more than $50nm$. Such structures with 20 layers that have an $55nm$ interlayer distance of vertically coupled $In_{0.5}Ga_{0.5}As/GaAs$ QDs were grown [33] experimentally by molecular beam epitaxy. In our case, the medium with a length of $55\mu m$ will consists of approximately 25 layers.

To generate the transition $|0\rangle\leftrightarrow|1\rangle$, a weak and incoherent probe field with Rabi frequency $\Omega_p=E_p\mu_{01}/\hbar$ has been passed through the considered QDs ensemble, where E_p is the amplitude of the probe field, and μ_{01} is the dipole transition moment of $|0\rangle\leftrightarrow|1\rangle$. For the interband transitions, the dipole moment is equal to $\mu_{01}=6.4\cdot10^{-29}\,C\,m$ for $InAs/GaAs$ QDs [34]. Besides the probe field, a coupling field with about $2720nm$ wavelength and periodical intensity distribution illuminates the medium. This field can be formed from the superposition of two coherent fields which interfere with each other

Preprints (www.preprints.org) | NOT PEER-REVIEWED | Posted: 27 December 2022 doi:10.20944/preprints202212.0505.v1

to create intensity distribution with periodically modulated Rabi frequency $\Omega_c = \Omega_{c0}\cos(\pi x/d)$. Here d is the spatial period of the intensity distribution which depends on the angle between two intersecting beams. Thus, by changing the angle you can smoothly manipulate the period of the intensity distribution.

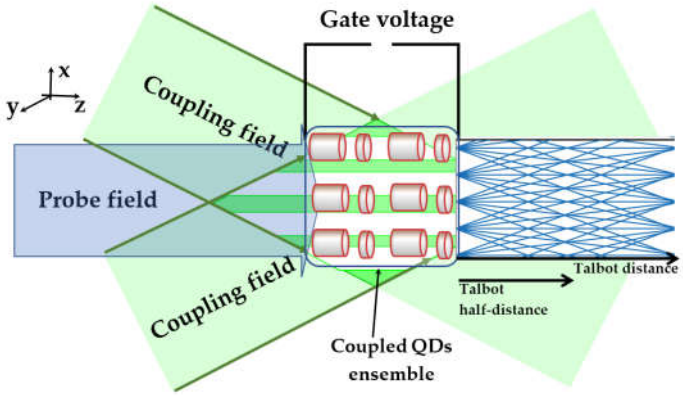

Figure 5. A possible scheme for Talbot effect's formation from vertically coupled QDs ensemble. Two coupling beams interfere with each other by forming intensity distribution with periodically modulated Rabi frequency. Probe field passing through vertically coupled QDs system diffracts and forms Talbot carpet.

In the proceeding calculations, we will use the following notation: Γ_1, Γ_3 - the spontaneous decay rates (lifetime broadening linewidth) from the $|1\rangle$ and $|3\rangle$ states respectively; $\delta_p = \omega_p + \omega_{10}$ - the differences between the probe field frequency and the frequency of the excited state transition; $\delta_c = \omega_c - \omega_{32}$ - the frequency difference between the coupling field and a related transition. Here ω_p is the angular frequency of the probe field, ω_c the angular frequency of the coupling field, T_e is the electron tunneling matrix element from the first QD to the second one, ω_{10} and ω_{32} are the angular frequencies that correspond to the transitions $|0\rangle \leftrightarrow |1\rangle$ and $|2\rangle \leftrightarrow |3\rangle$, respectively. The latter frequencies are defined by the difference of the energy states $\omega_{ij} = E_i - E_j$, at the same time ω_{21}, as well as T_e, can be tuned by the external electric field.

The interaction Hamiltonian in the matrix form between the vertically coupled QD system and the external electromagnetic fields in the electric-dipole and rotating-wave approximations have the following form [35,36]:

$$H = \begin{pmatrix} 0 & -\Omega_p e^{-i\delta_p t} & 0 & 0 \\ -\Omega_p^* e^{i\delta_p t} & 0 & T_e e^{i\omega_{12} t} & 0 \\ 0 & T_e e^{-i\omega_{21} t} & 0 & -\Omega_c e^{-i\delta_c t} \\ 0 & 0 & -\Omega_c^* e^{i\delta_c t} & 0 \end{pmatrix}. \quad (16)$$

As the next step, the standard density-matrix approach has been applied, in order to obtain the dynamics of the whole system. For the description of the time evolution of the system the following equations for the density matrix elements have been attained:

Preprints (www.preprints.org) | NOT PEER-REVIEWED | Posted: 27 December 2022 doi:10.20944/preprints202212.0505.v1

$$
\begin{aligned}
\dot{\rho}_{00} &= i\left(\rho_{10}\Omega_p - \rho_{01}\Omega_p^*\right) + \Gamma_1\rho_{11},\\
\dot{\rho}_{01} &= i\left(\left(\rho_{11} - \rho_{00}\right)\Omega_p + \delta_p\rho_{01} - \rho_{02}T_e\right) - \frac{\Gamma_1}{2}\rho_{01},\\
\dot{\rho}_{02} &= i\left(\left(\delta_p - \omega_{12}\right)\rho_{02} - \rho_{01}T_e + \rho_{12}\Omega_p - \rho_{03}\Omega_c^*\right),\\
\dot{\rho}_{03} &= i\left(\left(\delta_c + \delta_p - \omega_{12}\right)\rho_{03} - \rho_{02}\Omega_c + \rho_{13}\Omega_p\right) - \frac{\Gamma_3}{2}\rho_{03},\\
\dot{\rho}_{11} &= i\left(\rho_{01}\Omega_p^* + \left(\rho_{21} - \rho_{12}\right)T_e - \rho_{10}\Omega_p\right) - \Gamma_1\rho_{11},\\
\dot{\rho}_{12} &= i\left(\left(\rho_{22} - \rho_{11}\right)T_e - \omega_{12}\rho_{12} + \rho_{02}\Omega_p^* - \rho_{13}\Omega_c^*\right) - \frac{\Gamma_1}{2}\rho_{12},\\
\dot{\rho}_{13} &= i\left(\left(\delta_c - \omega_{12}\right)\rho_{13} + \rho_{03}\Omega_p^* + \rho_{23}T_e + \rho_{12}\Omega_c\right) - \frac{\left(\Gamma_1 + \Gamma_3\right)}{2}\rho_{13},\\
\dot{\rho}_{22} &= i\left(\left(\rho_{12} - \rho_{21}\right)T_e + \rho_{32}\Omega_c - \rho_{23}\Omega_c^*\right) + \Gamma_3\rho_{33},\\
\dot{\rho}_{23} &= i\left(\left(\rho_{33} - \rho_{22}\right)\Omega_c - \delta_c\rho_{23} + \rho_{13}T_e\right) - \frac{\Gamma_3}{2}\rho_{23},\\
\dot{\rho}_{33} &= -\left(\dot{\rho}_{00} + \dot{\rho}_{11} + \dot{\rho}_{22}\right).
\end{aligned}
\tag{17}
$$

The electric complex susceptibility χ is proportional to the coherence term ρ_{10} that, in the case of $\delta_c = \omega_{12} = 0$ and $\delta_p = 0$, can be presented in the following form [21]:

$$
\chi = \frac{N|\mu|^2}{2\hbar\varepsilon_0\Omega_p}\rho_{10} = \frac{N|\mu|^2}{2\hbar\varepsilon_0}\frac{i\Omega_{c0}^2\cos^2\left(\pi x/d\right)}{\Gamma_3 T_e^2 + \Gamma_1\Omega_{c0}^2\cos^2\left(\pi x/d\right)},
\tag{18}
$$

where N is the density number of the QD ensemble. As it is known the real and imaginary parts of electric susceptibility can define nonlinear changes in the refractive index and absorption coefficient of the medium, respectively:

$$
\delta n = \frac{16\pi^2}{\varepsilon_0 c}\operatorname{Re}\chi,
\tag{19}
$$

$$
\alpha_2 = \frac{32\pi^2\omega}{\varepsilon_0 c^2}\operatorname{Im}\chi.
\tag{20}
$$

Let us investigate the nonlinear changes in refractive index and absorption spectrum for different values of the tunneling parameters of the vertically coupled QDs ensemble.

Figures 6a and 6b show the dependences of the χ complex electric susceptibility's real ∂n and imaginary α_2 parts, respectively, on δ_p for $T_e = 0$ (solid red line), $T_e = 0.5\Gamma$ (blue dashed line), and $T_e = \Gamma$ (black dotted line) when $\Gamma_1 = \Gamma_2 = \Gamma$, $\Omega_c = 0.5\Gamma$, $\Omega_p = 0.4\Gamma$ and $\delta_c = 0$. We would like to highlight that Ω_c, Ω_p, δ_p and T_e are scaled to Γ. It is clear that when there is no tunneling effect ($T_e = 0$, solid red line in both a) and b)) excited electron is not able to pass from the left QD to the right one.

Preprints (www.preprints.org) | NOT PEER-REVIEWED | Posted: 27 December 2022 doi:10.20944/preprints202212.0505.v1

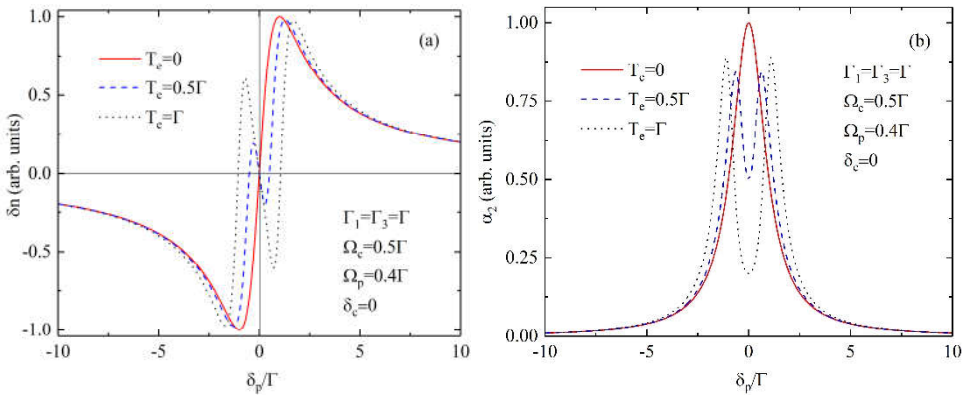

Figure 6. Nonlinear changes of the refractive index ∂n (a) and absorption coefficient α_2 (b) of the vertically coupled cylindrical QDs medium as a function of δ_p/Γ.

3.3. Tunneling-induced Talbot effect

Taking into account the fact that the electric susceptibility of the medium (QD ensemble) is periodically modulated along the x direction, the refractive index will be modulated as well. And the probe field passing through the system will be diffracted by the medium that has periodically modulated refractive indices and form the Talbot carpet in the near field. Thus, the output probe field will have the periodic structure with the following form [21] which is explicitly dependent on the tunneling parameter:

$$I_p(z=L) = I_0^2 \exp\left(\frac{-k_p\Omega_{c0}^2\cos^2(\pi x/d)L}{\Gamma_4 T_e^2 + \Gamma_2\Omega_{c0}^2\cos^2(\pi x/d)}\right), \tag{21}$$

where L is the length of the QDs medium and I_0^2 is the constant amplitude of the input probe beam. The visibility of the intensity pattern of the output probe beam can be expressed [21]:

$$V = \frac{1-\exp(-k_p L\Omega_{c0}^2/(\Gamma_4 T_e^2 + \Gamma_2\Omega_{c0}^2))}{1+\exp(-k_p L\Omega_{c0}^2/(\Gamma_4 T_e^2 + \Gamma_2\Omega_{c0}^2))}. \tag{22}$$

QD system serves as a diffraction grating for the probe beam, which at the Z distance from the surface of the system has a distribution of the following form:

$$\psi_p(X,Z) = \frac{e^{ik_p Z}}{\sqrt{\lambda_p Z}}\int_{-\infty}^{+\infty} E_p(x,L)\exp\left\{ik_p\frac{(x-X)^2}{2Z}\right\}dx, \tag{23}$$

where X and x are the coordinates in the observation plane and object. Because of the periodical behavior of χ (15), the Equation (19) can be written in the following way [37]:

$$\psi_p(X,Z) \propto \sum_{-\infty}^{+\infty} C_n \exp\left\{-i\frac{\pi\lambda_p n^2 Z}{d^2}\right\}\exp\left\{i\frac{2n\pi X}{d}\right\}. \tag{24}$$

C_n is the Fourier coefficient. Talbot planes which are self-imaging planes of the output probe beam are situated at $Z_T = 2md^2/\lambda_p$, where $m = 1,2,...$ is an integer number. The Talbot images at fractional Talbot distances are shifted by half period compared to the Talbot planes. For our system, the Talbot distance was estimated to be around $Z_T = 10mm$.

As the next step, we observed the influence of the tunneling effect on the Talbot effect generation in our system. Firstly, the visibility of the formed periodically modulated intensity pattern can be investigated from Equation 19. In Figure 7a we have plotted the formed periodic intensity pattern's visibility as a function of medium length L for different values of $\Omega_c = 0.25\Gamma, 0.5\Gamma, 0.75\Gamma, \Gamma$ in case of $\Gamma_1 = \Gamma_3 = \Gamma$ and $T_e = \Gamma$. It has become clear that with higher values of the coupling field's strength Ω_c the visibility reaches its max value of 1 faster. And Figure 7a allows the estimation of the optimal parameters for the medium length for obtaining a more visible Talbot effect.

Preprints (www.preprints.org) | NOT PEER-REVIEWED | Posted: 27 December 2022 doi:10.20944/preprints202212.0505.v1

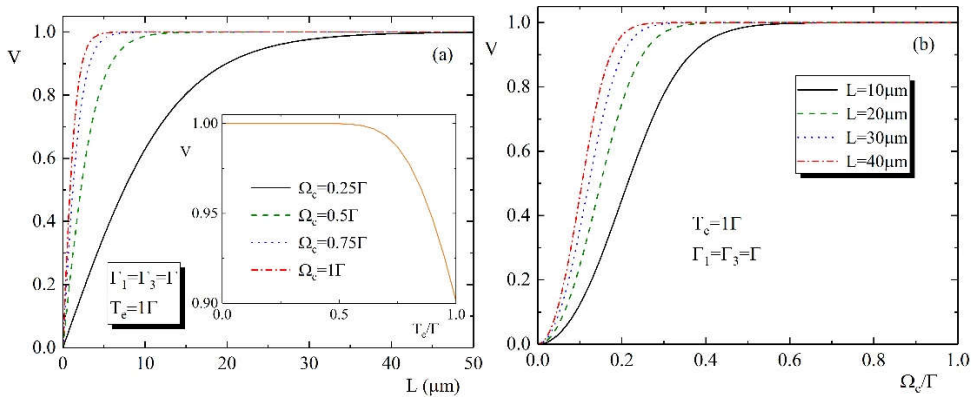

Figure 7. The dependences of the formed periodic wave front's visibility on medium length L (a) and coupling field's strength Ω_c/Γ (b) for different values of $\Omega_c = 0.25\Gamma, 0.5\Gamma, 0.75\Gamma, \Gamma$ and $L = 10\mu m, 20\mu m, 30\mu m, 40\mu m$ for the case of $\Gamma_1 = \Gamma_3 = \Gamma$ and $T_e = \Gamma$. The dependences of the visibility on tunneling parameter T_c/Γ can be seen in the left inset.

It is obvious from (19) that the visibility of the intensity pattern at the output of the ensemble being dependent on the tunneling parameter decreases with its greater values. The dependence of the visibility on the tunneling parameter can be seen in the inset of Figure 7a. It shows that the tunneling effect combined with the unit value of visibility induces the periodic pattern for the probe field. Nevertheless, as inferred from Equation 19, increasing the tunneling parameter causes the produced periodic waveform to become less visible. The induced periodic waveform has the highest value of visibility because small values of the tunneling parameter result in exactly zero values for the absorption at the coupling field's distribution nodes and absorption peaks at its anti-nodes. Furthermore, raising the tunneling parameter's value causes the tunneling-induced transparency to have wider line widths, which reduces the output probe field's visibility.

The visibility was plotted also as a function of the coupling field's strength (Figure 7b) for different values of medium length $L = 10\mu m, 20\mu m, 30\mu m, 40\mu m$ in the case of $\Gamma_1 = \Gamma_3 = \Gamma$ and $T_e = \Gamma$. A high visibility periodic pattern may be resulted by increasing the coupling field's strength. Figure 7b confirms this behavior for the pattern visibility. It is shown that by adjusting the following parameters: medium length L, the tunneling parameter, and the coupling field's strength; it is possible to obtain a high-resolution periodic pattern with a reduced period step whose visibility is entirely controlled.

3.4. Observation of Talbot carpet

For achieving Talbot carpet from a medium obtained from a cylindrical coupled QD ensemble the tunneling-induced transparency occurs (see Figure 7b). As the coupling field has periodical intensity distribution the absorption of the medium as a whole will also have a periodical character. Thus, the probe field passing through the tunneling-induced periodically transparent medium will be diffracted and a Talbot carpet will be formed at the near field (Figure 8). Taking into account that for the realization of inter-band transitions in $InAs/GaAs$ (see Section 2) the wavelength of the field should be near 2700nm we will use a resonant probe field. For further calculations, the period of the periodically modulated coupling field d was assumed 50μm which defines the Talbot distance near 11mm deriving from the $Z_T = 2md^2/\lambda_p$ expression. The simulation showed that in the case where the tunneling effect $T_e = 0$ is absent the Talbot carpet was not observed. Thus, the carpet is simulated in the case of the maximum value of the tunneling parameter $T_e = \Gamma$ (Figure 8). In the figure, we clearly can see the Talbot images at Talbot half-distances. Moreover, we can discern the revivals of Talbot sub-images shifted with doubled, tripled, and quadrupled frequencies in Figure 8 at $Z_T/2$, $Z_T/3$, $Z_T/4$ distanc-

Preprints (www.preprints.org) | NOT PEER-REVIEWED | Posted: 27 December 2022 doi:10.20944/preprints202212.0505.v1

es. It is shown that revivals at half-distances exhibit phase shifts which are typical for the Talbot phenomenon.

We have plotted the diffracted field's three-dimensional amplitude and intensity distributions (blue and orange curvatures in Figure 9, respectively) from the coupling field's strength Ω_{c0}/Γ for a more precise investigation of the probe field and its diffraction pattern at Talbot half-distance $Z_T/2$. The medium length is assumed $L = 25\mu m$ and the tunneling parameter has the maximum value $T_e = \Gamma$. The diffracted field's amplitude/intensity distribution shows that with the decrease of the coupling field's strength parameter the diffraction from the system disappears. Note, that the amplitude and intensity plotted in Figure 9 do not reach the minimum and maximum values on the vertical axes and a small gap exists. It means that the contrast of the carpet is not 100%.

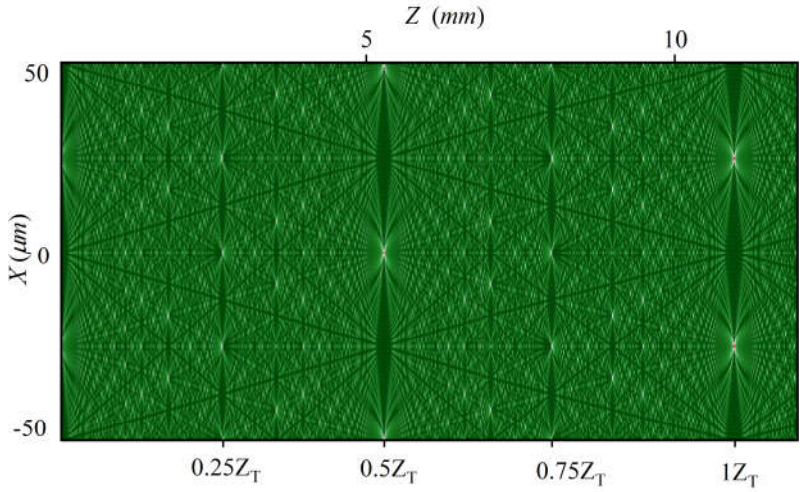

Figure 8. The formation of Talbot carpet from vertically coupled cylindrical QDs ensemble for the maximum value of tunneling parameter $T_e = \Gamma$ and $d = 50\mu m$, $Z_T = 10mm$.

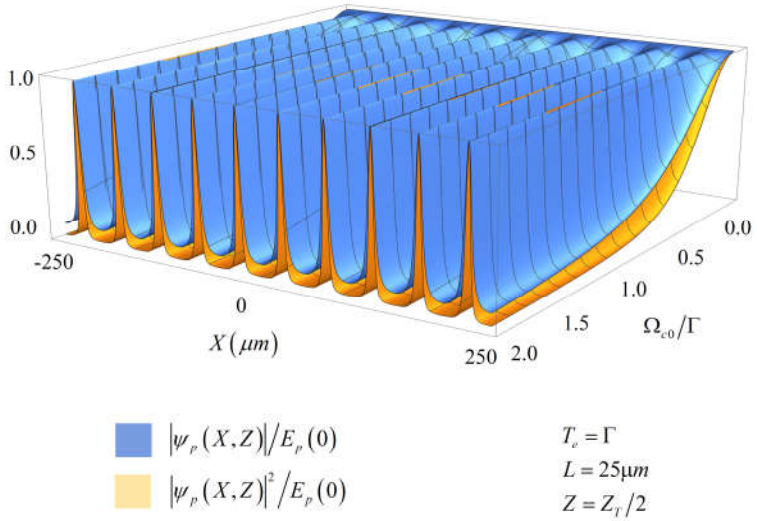

Figure 9. The amplitude and intensity distribution (blue and orange curvatures) of diffraction field at Talbot half-distance $Z_T/2$ for $L = 25\mu m$, $T_e = \Gamma$.

4. Conclusions

Summarizing all above-mentioned, the Talbot effect was shown in a *InAs*/*GaAs* vertically coupled cylindrical QD ensemble illuminated by the probe and periodically modulated coupling fields. The coupled QDs were modeled using the double MPTP, this model has made it possible to control the depth, the width and the interdot distance.

 doi:10.20944/preprints202212.0505.v1

The exciton states were considered in these systems in the presence of an external electric field. The nonlinear refractive index changes and the nonlinear absorption coefficients were calculated for different values of the tunneling parameters. The exciton lifetime and tunneling time are calculated directly: exciton lifetime lies in the *ns* range, while the tunneling time is in the *ps* range. The exciton lifetime's dependence on the half-width of the first QD displayed a linear growth, while tunneling time's dependence on the same parameter exhibited an exponential decrease. Note, that dependence of the tunneling time on the electric field had a clear $\exp(-1/F_z)$ form.

The influence of the tunneling on Talbot effect formation was observed in our system. It was shown that the tunneling effect combined with the unit value of visibility induced the periodic pattern of the probe field. Nevertheless, increasing the tunneling parameter caused the periodic waveform to become less visible. The induced periodic waveform had the highest value of visibility because small values of the tunneling parameter resulted in exactly zero values for the absorption at the coupling field's distribution nodes and absorption peaks at its anti-nodes. Furthermore, raising the tunneling parameter's value caused the tunneling-induced transparency to have wider line widths, which reduced the output probe field's visibility.

It became clear that by adjusting the QDs ensemble medium length, tunneling parameter, and coupling field's strength, we may offer a high-resolution periodic pattern with a reduced period step whose visibility was completely controllable.

Author Contributions: G.A.M., D.B.H. – numerical calculations, P.A.M. and D.B.H. conceptualization and development of the theory, G.AM and P.A.M. original draft preparation, review, and editing.

Funding: The work was supported by the Science Committee of RA, in the frames of the research project № 21SCG-1C008.

Conflicts of Interest: The authors declare no conflict of interest. The funders had no role in the design of the study; in the collection, analyses, or interpretation of data; in the writing of the manuscript, or in the decision to publish the results.

References

1. Talbot, H. F. Facts relating to optical science. *Philosophical Magazine* **1836**, *9*, 401–407.
2. Isoyan, A.; Jiang, F.; Cheng, Y. C.; Cerrina, F.; Wachulak, P.; Urbanski, L.; Rocca, J.; Menoni, C.; Marconi, M. Talbot lithography: Self-imaging of complex structures. *Journal of Vacuum Science & Technology B: Microelectronics and Nanometer Structures Processing, Measurement, and Phenomena* **2009**, *27(6)*, 2931-2937.
3. Coulon, P. M.; Damilano, B.; Alloing, B.; Chausse, P.; Walde, S.; Enslin, J.; Armstrong, J.; Vézian, R.; Hagedorn, S.; S., Wernicke, T. and Massies, J. Displacement Talbot lithography for nano-engineering of III-nitride materials. *Microsystems & Nanoengineering* **2019**, *5(1)*, 1-12.
4. Nakano, Y.; Murata, K. Talbot interferometry for measuring the focal length of a lens. *Applied optics* **1985**, *24(19)*, 3162-3166.
5. Yang, G.; Miao, L.; Zhang, X.; Sun, C.; Qiao, Y. High-accuracy measurement of the focal length and distortion of optical systems based on interferometry. *Applied Optics* **2018**, *57(18)*, 5217-5223.
6. Farias, O. J.; de Melo, F.; Milman, P.; Walborn, S. P. Quantum information processing by weaving quantum Talbot carpets. *Physical Review A* **2015**, *91(6)*, 062328.
7. Tsarev, M. V.; Ryabov, A.; Baum, P. Free-electron qubits and maximum-contrast attosecond pulses via temporal Talbot revivals. *Physical Review Research* **2021**, *3(4)*, 043033.
8. Zhang, Y.; Wen, J.; Zhu, S. N.; Xiao, M. Nonlinear talbot effect. *Physical Review Letters* **2010**, *104(18)*, 183901.
9. Zhao, X.; Yuanlin Zh; Huaijin R.; Ning A.; Xianfeng Ch. Cherenkov second-harmonic Talbot effect in one-dimension nonlinear photonic crystal. *Optics letters* **2014**, *39*, 885-5887.
10. Salas, J. A.; Varga, K.; Yan, J. A.; Bevan, K. H. Electron Talbot effect on graphene. *Physical Review B* **2016**, *93(10)*, 104305.
11. Badalyan, A.; Hovsepyan, R.; Mekhitaryan, V.; Mantashyan, P.; Drampyan, R. Talbot effect from rotational symmetry gratings: Application to 3D refractive grating formation. *Molecular Crystals and Liquid Crystals* **2012**, *561(1)*, 57-67.
12. Höllmer, P.; Bernier, J. S.; Kollath, C.; Baals, C.; Santra, B.; Ott, H. Talbot effect in the presence of interactions. *Physical Review A* **2019**, *100(6)*, 063613.
13. Bajwa, N.; Mehra, N. K.; Jain, K.; Jain, N. K. Pharmaceutical and biomedical applications of quantum dots. *Artificial cells, nanomedicine, and biotechnology* **2016**, *44(3)*, 758-768.
14. Sun, B.; Ouellette, O.; García de Arquer, F. P.; Voznyy, O.; Kim, Y.; Wei, M.; Proppe, A.H.; Saidaminov, M.I.; Xu, J.; Liu, M.; Li, P. Multibandgap quantum dot ensembles for solar-matched infrared energy harvesting. *Nature communications* **2018**, *9(1)*, 1-7.

15. Huang, Y. M., Singh, K. J., Liu, A. C., Lin, C. C., Chen, Z., Wang, K., Lin, Y., Liu, Z., Wu, T. and Kuo, H.C. Advances in quantum-dot-based displays. *Nanomaterials* **2020**, *10(7)*, 1327.
16. Yao, R.; Lee, C. S.; Podolskiy, V.; Guo, W. Single-transverse-mode broadband InAs quantum dot superluminescent light emitting diodes by parity-time symmetry. *Optics Express* **2018**, *26(23)*, 30588-30595.
17. Kagan, C. R.; Bassett, L. C.; Murray, C. B.; Thompson, S. M. Colloidal quantum dots as platforms for quantum information science. *Chemical reviews* **2020**, *121(5)*, 3186-3233.
18. Liu, H. Y.; Xu, B.; Wei, Y. Q.; Ding, D.; Qian, J. J.; Han, Q.; Liang, J.B.; Wang, Z. G. High-power and long-lifetime InAs/GaAs quantum-dot laser at 1080 nm. *Applied Physics Letters* **2001**, *79(18)*, 2868-2870.
19. Fafard, S.; Wasilewski, Z. R.; Allen, C. N.; Picard, D.; Spanner, M.; McCaffrey, J. P.; Piva, P. G. Manipulating the energy levels of semiconductor quantum dots. *Physical Review B* **1999**, *59(23)*, 15368.
20. Fafard, S.; Spanner, M.; McCaffrey, J. P.; Wasilewski, Z. R. Coupled InAs/GaAs quantum dots with well-defined electronic shells. *Applied Physics Letters* **2000**, *76(16)*, 2268-2270.
21. Azizi, B.; Amini Sabegh, Z.; Mahmoudi, M.; Rasouli, S. Tunneling-induced Talbot effect. *Scientific Reports* **2021**, *11(1)*, 1-14.
22. Li, S.S.; Xia, J.B.; Yuan, Z.L.; Xu, Z.Y.; Ge, W.; Wang, X.R.; Wang, Y.; Wang, J.; Chang, L.L. Effective-mass theory for InAs/GaAs strained coupled quantum dots. *Physical review B* **1996,** *54(16)*, 11575.
23. Sargsian, T.A.; Mkrtchyan, M.A.; Sarkisyan, H.A.; Hayrapetyan, D.B. Effects of external electric and magnetic fields on the linear and nonlinear optical properties of InAs cylindrical quantum dot with modified Pöschl-Teller and Morse confinement potentials. *Physica E: Low-dimensional Systems and Nanostructures* **2021**, 126, 114440.
24. Hayrapetyan, D.B.; Kazaryan, E.M.; Tevosyan, H.K. Direct interband light absorption in the cylindrical quantum dot with modified Pöschl–Teller potential. *Physica E: Low-dimensional Systems and Nanostructures* **2012**, 46, 274-278.
25. Sargsian, T.A.; Mantashyan, P.A.; Hayrapetyan, D.B. Effect of Gaussian and Bessel laser beams on linear and nonlinear optical properties of vertically coupled cylindrical quantum dots. *Nano-Structures & Nano-Objects* **2023**, 33, 100936.
26. Barker, J.A.; O'Reilly, E.P. The influence of inter-diffusion on electron states in quantum dots. *Physica E: Low-dimensional Systems and Nanostructures* **1999**, 4, 231-237.
27. Fonoberov, V.A.; Balandin, A.A. Origin of ultraviolet photoluminescence in ZnO quantum dots: confined excitons versus surface-bound impurity exciton complexes. *Applied physics letters*. **2004**, 85, 5971-5973.
28. Vurgaftman, I.; Meyer, J.Á.; Ram-Mohan, L.Á. Band parameters for III–V compound semiconductors and their alloys. *Journal of applied physics*. **2001**, 89, 5815-5875.
29. Villas-Bôas, J.M.; Ulloa, S.E.; Govorov, A.O. Decoherence of Rabi oscillations in a single quantum dot. *Physical review letters*. **2005**, 94, 057404.
30. Müller, K. et al. Electrical control of interdot electron tunneling in a double InGaAs quantum-dot nanostructure. *Physical review letters*. **2012**, 108, 197402.
31. Bleyan, Y.Y.; Mantashyan, P.A.; Kazaryan, E.M.; Sarkisyan, H.A.; Accorsi, G.; Baskoutas, S.; Hayrapetyan, D.B. Non-Linear Optical Properties of Biexciton in Ellipsoidal Quantum Dot. *Nanomaterials*. **2022**, 12, 1412.
32. Hayrapetyan, D.B.; Bleyan, Y.Y.; Baghdasaryan, D.A.; Sarkisyan, H.A.; Baskoutas, S.; Kazaryan, E.M. Biexciton, negative and positive trions in strongly oblate ellipsoidal quantum dot. *Physica E: Low-dimensional Systems and Nanostructures*. **2019**, 105, 47-55.
33. Yu, P.; Langbein, W.; Leosson, K.; Hvam, J. M.; Ledentsov, N. N.; Bimberg, D.; Ustinov, V. M.; Egorov, A. Yu.; Zhukov, A. E.; Tsatsul'nikov, A. F.; Musikhin, Y. G. Optical anisotropy in vertically coupled quantum dots. *Physical Review B* **1999**, 60(24), 16680.
34. Jin, P.; Li, C.M.; Zhang, Z.Y.; Liu, F.Q.; Chen, Y.H.; Ye, X.L.; Xu, B.; Wang, Z.G. Quantum-confined Stark effect and built-in dipole moment in self-assembled InAs⁄GaAs quantum dots. *Applied physics letters*. **2004**, 85, 2791-2793.
35. Agarwal, G. S. *Quantum optics*. Cambridge University Press, 2012.
36. Scully, M. O.; Zubairy, M. S. *Quantum optics*, 1999.
37. Wen, J., Du, S., Chen, H., & Xiao, M. Electromagnetically induced Talbot effect. *Applied Physics Letters*. **2011,** 98(8), 081108.